Enhanced interfacial deformation in a Marangoni flow: A measure of the dynamical surface tension

Rodrigo Leite Pinto, Sébastien Le Roux, Isabelle Cantat, and Arnaud Saint-Jalmes

Univ Rennes, CNRS, IPR (Institut de Physique de Rennes) - UMR 6251, F-35000 Rennes, France

We investigate the flows and deformations resulting from the deposition of a water soluble surfactant at a bare oil-water interface. Once the surfactant is deposited, we show that the oil-water interface is deformed with a water bump rising upward into the oil. For a given oil, the maximal deformation—located at the surfactant deposition point—decreases with the oil-layer thickness. We also observe a critical oil-layer thickness below which the deformation becomes as large as the oil layer, leading to the rupture of this layer and an oil-water dewetting. Experimentally, it is found that this critical thickness depends on the oil density and viscosity. We then provide an analytical modelization that explains quantitatively all these experimental features. In particular, our analysis allows us to derive an analytical relationship between the vertical profile of the oil-water interface and the in-plane surface tension profile. Therefore, we propose that the monitoring of the interface vertical shape can be used as a new spatially resolved tensiometry technique.

I. INTRODUCTION

As a consequence of a surface tension gradient, a bulk flow emerges to compensate this tangential stress: this is known as the Marangoni effect [1,2]. In practice, various actions can be used to trigger a nonuniform interfacial tension. For instance, a spatially limited heating of the interface decreases locally the interfacial tension, which consequently creates thermocapillary flows [3–7]. As well, by depositing a small amount of amphiphilic molecules (or surfactant) at an interface between two phases, a gradient of concentration is created, and so a gradient of surface tension. In the simplest case of a water-air interface and for insoluble surfactants, the spreading of the monolayer at the interface is accompanied by a sharp deformation of the interface and a front that propagates away from the source. Experiments and simulations have especially focused on the scaling regimes describing the position of this front with time [8–11].

In the case of soluble surfactants, the situation is more complex, though more relevant if one considers many natural and industrial processes. Here, the concentration close to the interface is a dynamical quantity, governed by the convection-diffusion equation. This concentration sets the local value of the surface tension, and thus the viscous tangential stress at the interface, which is the driving force for the flow. This coupling between bulk and interface leads to a large variety of dynamical behaviors, all associated to a surfactant supply at a liquid interface, such as spreading [12–17], self-propulsion [18,19], oscillation [20], dynamical dewetting [21], instabilities [22–24], or droplets emission [25]. In fact, there are many issues on such surfactant-assisted Marangoni flows that need to be tackled. For instance, to understand these various behaviors, accurate measurements of the interfacial and bulk concentration fields are required; in particular, local and direct measurements of the out-of-equilibrium surface tension are still lacking.

In this article, our goal is to go beyond the usual liquid-gas interface, by replacing the infinite top air layer by a finite viscous oil one. This is motivated by the fundamental question of surfactant transport on flowing interfaces but also by the need to better control the dynamical effects occurring within emulsions and in confined multiphasic flows (like in microfluidic chips). Therefore, we focus

here on the dynamics induced when a drop of a concentrated solution of water-soluble surfactant is deposited at a stable interface between oil and pure water. Macroscopic features, easily visible with the naked eye, are then triggered. The oil-water interface is strongly deformed, and we show that the interface deformation decreases with the oil-layer thickness. Experimentally, we also find a critical thickness, separating situations where the deformation is big enough to pierce the oil layer (dewetting cases), from situations where the water layer remains covered by oil (no-dewetting cases). Then we propose a model quantitatively explaining our observations. Interestingly, we show that the height of the oil-water interface at any given point is related to the value of the surface tension at the same point by a simple analytical expression. We evidence that, for all the oil-layer thicknesses we tested, the maximal height reached by the oil-water interface at the injection point is in quantitative agreement with this expression, computed using the surface tension imposed locally by the drop, which is known. Our model can then be used to deduce the local surface tension from the interface deformation, anywhere on the interface. In our geometry, we thus propose a new spatially resolved tensiometry technique based on the optical measurement of the interface deformation, which may be suited to other Marangoni flows.

II. EXPERIMENTAL SETUP

The experiment is performed in a parallelepipedic tank ($25.5 \times 45.5 \times 25$ cm^3) initially filled with several liters of ultra pure water (Millipore range), leading to a water layer thickness H of the order of 10 cm.

A controlled volume of sunflower oil is then poured to produce an oil film of thickness d in the range [3–13] mm at the surface of the water. The oil and water phases are denoted respectively by phase 1 and phase 2 in the following (see Fig. 1, top). Complementary experiments are also done
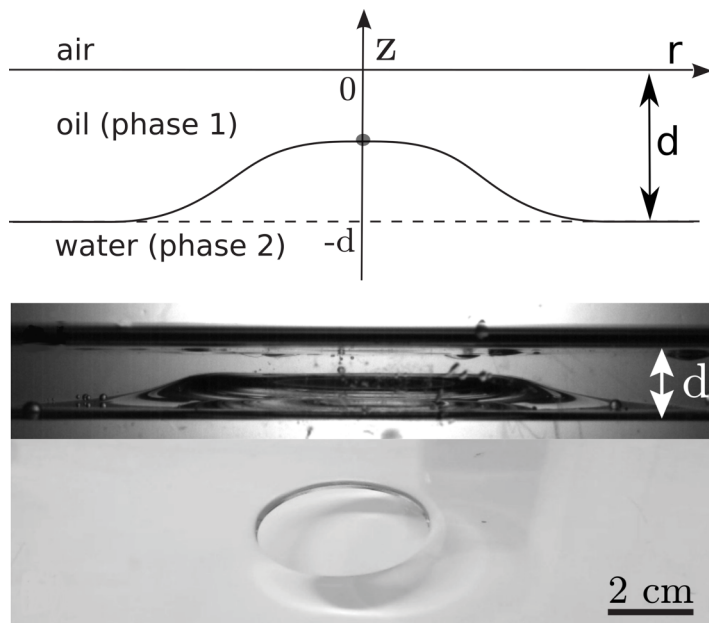

FIG. 1. Top: Schematic of the experiment, side view. The gray dot represents the surfactant drop, deposited on the initially flat oil-water interface; after the drop coalesces with the water bath, the oil-water interface deforms upwards. Middle: Picture of the experiment, side view. The upward deformation of the oil-water interface is visible, and the height of the deformation is smaller than the oil-layer thickness d (no dewetting case). Bottom: Picture of the experiment, top view. In that case the oil-water interface has touched the oil-air interface and a hole in the oil layer appears, visible in the image (dewetting case).

TABLE I. Physicochemical properties of the water and sunflower oil phases and geometrical control parameters.

		ρ_2	$1000\,\mathrm{kg\,m^{-3}}$
	Water	η_2	$1\,\mathrm{mPa\,s}$
Fluids		ρ_1	$920\,\mathrm{kg\,m^{-3}}$
	Oil	η_1	$50\,\mathrm{mPa\,s}$
	Oil d		$[3\text{–}13]\,\mathrm{mm}$
Geometry	Water H		$10\,\mathrm{cm}$
	γ_{OA}		$32\,\mathrm{mN\,m^{-1}}$
	γ_{OW}		$25\,\mathrm{mN\,m^{-1}}$
Interfaces	$\gamma_0 = \gamma_{\mathrm{O(W+SDS)}}$		$1\,\mathrm{mN\,m^{-1}}$
	$\Delta\gamma = \gamma_{\mathrm{OW}} - \gamma_0$		$24\,\mathrm{mN\,m^{-1}}$

with a silicone oil (V10) and with hexadecane, for comparisons to the sunflower oil results, to check the role of the water-oil density and viscosity ratio.

For the sunflower oil, the surface tensions γ_{OA} and γ_{OW}, respectively, at the oil-air and oil-water interfaces, are measured by the pendant drop technique and given in Table I. The spreading coefficient of the oil on water is $S = \gamma_{\mathrm{WA}} - (\gamma_{\mathrm{OA}} + \gamma_{\mathrm{OW}}) = 15\,\mathrm{mN/m}$, with $\gamma_{\mathrm{WA}} = 72\,\mathrm{mN/m}$ the surface tension of pure water. This coefficient is positive, which is consistent with the spontaneous spreading of the oil experimentally observed, for every oil thickness (as for the two other oils).

The spreading coefficient is still positive when surfactant is added in the water phase, and the oil layer is thus always thermodynamically stable. The oil density ρ_1 is smaller than the water density ρ_2, as shown is Table I, so the two liquid layers are stable in the gravity field.

The experiment consists in the deposition of a drop of a concentrated aqueous solution of sodium dodecyl sulfate (SDS) just above the oil-water interface, without initial velocity. The drop volume is $20\,\mu\mathrm{l}$, unless otherwise specified, and the concentration is $c = 15$ cmc (where cmc is the critical micellar concentration, and equal to 8 mM for SDS). After a small delay, the drop coalesces with the pure water phase and suddenly sets the system in an out-of-equilibrium state. The SDS concentration in the water close to the drop coalescence point becomes larger than the cmc, which locally lowers the oil-water surface tension to its minimal value. Using a pendant drop apparatus, an independent measurement of this surface tension above the cmc provides $\gamma_0 = 1\,\mathrm{mN/m}$.

The shape of the oil-water interface is recorded at 125 images/s with a Photron Fastcam set on the side of the tank, and mounted with a 50-mm Nikon camera lens. The system is lighted in transmission with a Phlox light covered by a diffusing sheet (see Fig. 1, middle). The oil-water interface deformation is then determined by image processing. In some cases, both phases have been seeded with particles to observe qualitatively the velocity fields [26]. Additional images have been recorded with a different angle to see the oil-air interface from the top (see Fig. 1, bottom).

III. EXPERIMENTAL RESULTS

A. Time evolution of the oil-water interface

The most striking observation is that the oil-water interface is strongly deformed once the drop has coalesced: a bump of water rises up into the oil phase (see Fig. 1).

Bump profiles at different times are shown in Fig. 2. Note that after a transient during which the bump is growing, its height saturates to a constant value for several seconds, while the lateral extension begins to slowly decrease. Eventually the bump disappears in typically 1 s. Figure 3 presents this specific dynamics in more details.

The system remains axisymmetric and the oil-water deformation can be described with cylindrical coordinates by the function $h_2(r,t)$, with r the distance from the drop injection point, and $t = 0$ when
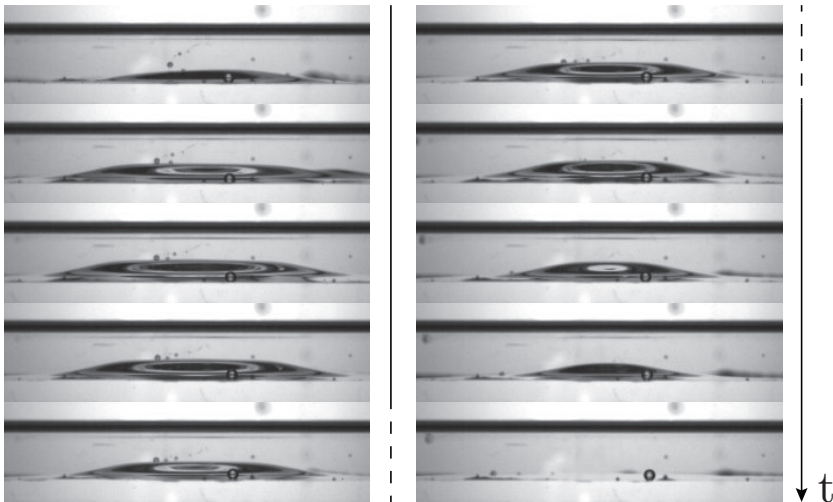
FIG. 2. Successive bump profiles at the water-oil interface. The delay between the images is 800 ms. In that case, the oil layer is thick enough ($d = 9.5$ mm) so that no dewetting occurs.

the drop coalesces with the water layer. The reference value at $t < 0$, as well as for large values of r, is $h_2(r,t) = 0$. The height $h_2(0,t)$ at the point of drop deposition is plotted in Fig. 3 (top) as a function of time t, for different oil-layer thicknesses. The error bar on this maximal value of $h_2(r,t)$ is 0.25 mm, corresponding to one pixel size. A well-defined plateau in the graph $h_2(0,t)$ lasts for a few seconds, and this plateau $h_{2,\max}$ has a larger value for thinner oil layers.

In Fig. 3 (bottom), we show the bump radius as a function of time for the same experiments. This typical radius is defined as the largest value of r for which a height variation is observable. As the transition is rather smooth, this value has a large uncertainty, of the order of 10%. The height and the radius first increase rapidly together, and when the height saturates at its plateau value, the radius begins to slowly decrease.

Another important result is that if the oil layer is thinner than a critical thickness d_c, the top of the bump reaches the oil-air interface. In that case a dynamically enforced dewetting is observed, as seen in Fig. 1, bottom. The behavior at short times is similar for $d > d_c$ and $d < d_c$, but in this latter case the bump height is limited by the oil-layer thickness. Dewetting has been reproducibly obtained for $d = 6.9$ mm and has never been obtained for $d = 8.7$ mm. We thus define the experimental value of the critical oil-layer thickness leading to the dewetting transition as $d_c^{\mathrm{exp}} = 8 \pm 1$ mm.

The velocity field has been qualitatively observed in both phases (see Supplemental Material [26]). The surface tension gradient at the oil-water interface induces an outward flow in the oil and in the water, close to the interface. A consequence of this flow is the increase of the pressure at large r, which leads to inwards counter flows in both phases: annular vortices are thus visible around the bump. The typical velocities, measured on a small set of particles trajectories followed by eyes, are of the order of $U_1 = 10^{-2}$ m s^{-1} in the oil phase, and of the order of $U_2 = 5.10^{-3}$ m s^{-1} in the water phase.

B. Maximal bump height for $d > d_c$

In the following, we focus on the maximal height $h_{2,\max}$ reached by the oil-water interface in the cases without dewetting. It is measured from the dynamical profile $h_2(r) = h_2(r,t^{pl})$ at a time t^{pl} in the middle of the height plateau. All the dynamical quantities discussed below are implicitly considered at that time. An example of such interface profile, obtained for $d = 8.7$ mm, is plotted in Fig. 4. It is rather flat in the middle and can be fitted by the phenomenological law,

$$h_2(r) = \frac{h_{2,\max}}{2}\left[1 - \tanh\left(\frac{r - r_0}{\alpha}\right)\right], \tag{1}$$
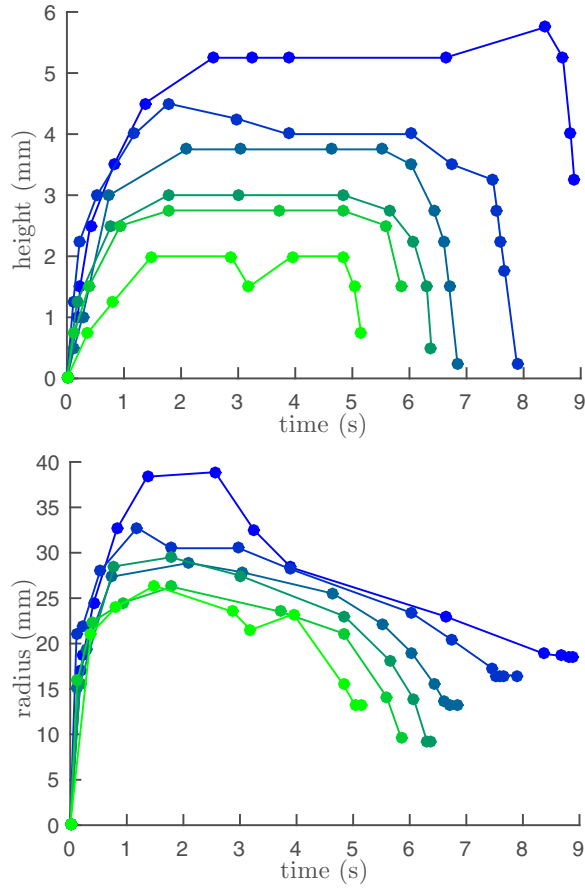
FIG. 3. Evolution of the oil-water interface shape as a function of time for different oil-layer thicknesses d, for $d > d_c$ (no dewetting). From top to bottom (and blue to green on line) $d = [8.7; 9.5; 10.4; 11.3; 12.1; 13]$ mm. (Top) Height of the bump $h_2(0,t)$ at the drop deposition point; (bottom) bump radius R.
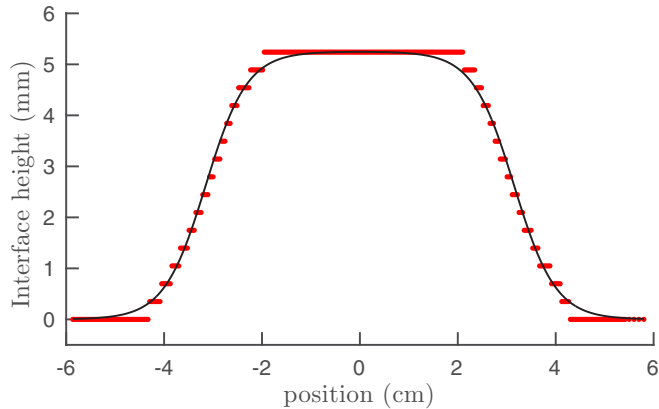

FIG. 4. Interface profile $h_2(r)$ for an oil-layer thickness $d = 8.7$ mm. The error bar is 0.25 mm, given by the pixel size. The black line is a phenomenological fit [Eq. (1)] with $h_{2,\text{max}} = 5.2$ mm, $\alpha = 8.5$ mm and $r_0 = 3.15$ cm.
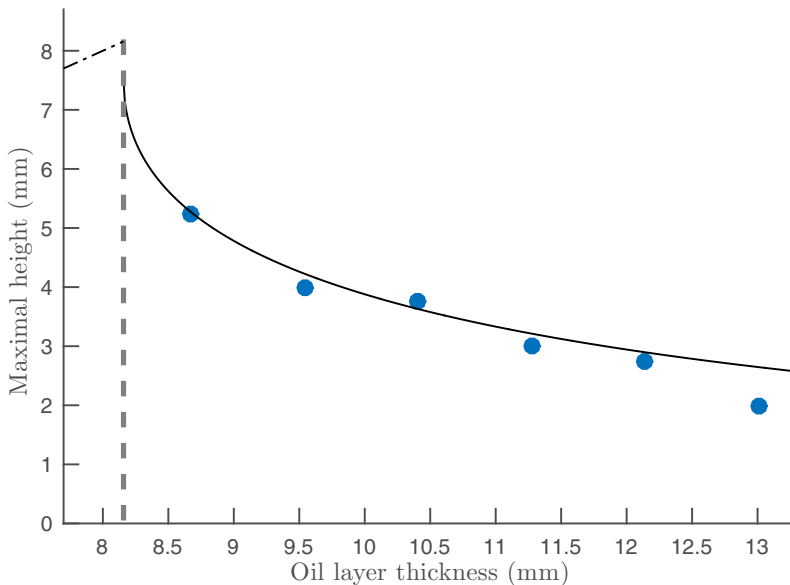
FIG. 5. Maximal height of the oil-water interface $h_{2,\text{max}}$ as a function of the oil-layer height d, in absence of dewetting. Dots: experimental data $h_{2,\text{max}}^{\text{exp}}$. Solid line: prediction $h_{2,\text{max}}^{th}$ of Eq. (21) without adjustable parameters; dot-dashed line: line $h_{2,\text{max}} = d$ obtained is case of dewetting (systematic dewetting is obtained for $d = 6.9\,\text{mm}$); dashed line: critical value d_c leading to the dewetting transition, given by Eq. (22) (and by the intersection of the solid and dot-dashed lines).

with α the characteristic lateral extension of the transition between $h_2 = h_{2,\text{max}}$ and $h_2 = 0$, and r_0 the lateral extension of the bump, close to the maximal experimental value of R (see Fig. 3, bottom). For a given oil, our main control parameter is the oil-layer thickness d, and the value of $h_{2,\text{max}}$ is reported as a function of d in Fig. 5. This height increases when the oil-layer height decreases, and thus becomes equals to d at a critical thickness $d = d_c$. This is at the origin of the dewetting transition corresponding to $h_{2,\text{max}} = d_c$.

IV. MODELIZATION

A. The quasisteady regime

Before writing rigorously the equations of motion in both phases, we first discuss qualitatively some important features involved in the bump formation. The total amount of surfactant brought by the drop is 2.4×10^{-6} mol. When the mixing of the drop into the 8 l of pure water is achieved, a concentration of the order of $3\ 10^{-7}$ mol/l is obtained, leading to no measurable surface tension variation at the oil-water interface. At large time the oil-water surface tension remains thus at its equilibrium value. However, as long as the droplet is not entirely spread, it maintains the interfacial surfactant concentration at its cmc value close to the coalescence point and the interface is locally saturated with surfactants.

At a distance r larger than R, in contrast, the interface remains bare at all times, as briefly discussed below on the basis of a previous study [16]. The Marangoni stress induced by the surface tension difference between $r = 0$ and $r = R$ leads to a fast convective spreading of the surfactant at the interface. The bulk concentration is significantly modified in a thin layer just below the interface, called the mass boundary layer. During their convective transport outwards, the surfactants also diffuse toward the deeper water phase, and the concentration near the interface thus decreases with r, until it reaches negligible values, at a distance R from the deposition point. The balance between
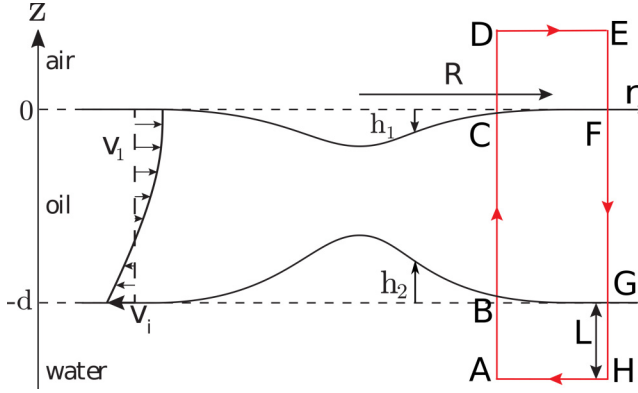
FIG. 6. Scheme of the studied system. The interface deformations verify $h_1 < 0$ (downward deformation) and $h_2 > 0$ (upward deformation). Due to the confinement the velocity in the oil phase is radial and its value $v_1(r,z)$ is schematized on the left.

surfactant injection by the droplet, convection by the interface velocity, and diffusion toward the water bulk determines the concentration field, and thus the local surface tension. In the following, the aim is not to predict this concentration field, but rather to focus on the coupling between the interface deformation and the surface tension distribution.

Before the drop dissolution, the global surface tension difference between the point of drop deposition and the boundary of the oil-water interface at large r is constant in time. We will show that this constant difference is at the origin of the stabilisation of the bump height at its maximal value, even if the spatial distribution of the surface tension, and especially the value of R, slightly evolves. We will call this regime the quasisteady regime.

We developed an axisymmetric model to predict the relationship between this dynamical surface tension distribution and the interface deformation during this quasisteady regime. The notations we use are given in Fig. 6. The relevant physicochemical quantities and geometrical characteristics are summarized in Table I, as well as the order of magnitude of the control parameters and dynamical quantities used to justify the assumptions of the model.

B. Flow in the oil phase

The flow in the oil phase occurs in a very flat domain of typical height $d \sim 10^{-3}$ m and typical lateral extension $R \sim 10^{-2}$ m. This justifies the use of the lubrication equation:

$$\eta_1 \frac{\partial^2 v_1}{\partial z^2} = \frac{\partial p_1}{\partial r}. \tag{2}$$

In this quasiparallel flow, the vertical pressure gradient is only controlled by the gravity force and $\partial_z p_1 = \rho_1 g$. The deformation of the oil-air interface is much smaller than the deformation of the oil-water interface and h_1 is at most of the order of 1 mm. The Laplace pressure jump at the interface scales as $\gamma_{\mathrm{OA}} h_1/R^2 \sim 10^{-2}$ Pa and is negligible in comparison with the hydrostatic pressure. The pressure at the position $z = h_1(r)$ is thus the atmospheric pressure, taken as the reference pressure. We deduce $p_1(z,r) = \rho_1 g (h_1(r) - z)$ and $\partial_r p_1 = \rho_1 g \, dh_1/dr$, so

$$\eta_1 \frac{\partial^2 v_1}{\partial z^2} = \rho_1 \, g \, \frac{dh_1}{dr}. \tag{3}$$

The tangential stress continuity at the two interfaces imposes:

$$\eta_1 \frac{\partial v_1}{\partial z} = 0 \quad \text{for } z = h_1, \tag{4}$$

$$\frac{d\gamma}{dr} + \eta_1 \frac{\partial v_1}{\partial z} - \eta_2 \frac{\partial v_2}{\partial z} = 0 \quad \text{for } z = -d + h_2. \tag{5}$$

At the oil-water interface, $v_2 = v_1 = v_i \sim 10^{-2}$ m/s. In the oil phase, the velocity gradient scales as v_i/d (or larger close to the dewettting transition) so $\eta_1 \partial v_1/\partial z \sim 5 \times 10^{-2}$ Pa. In the water phase, a viscous boundary layer is generated by the interfacial velocity, with a typical thickness $\ell_w = \sqrt{\eta_2 R/(\rho_2 v_i)} \sim 1$ mm. We thus have $\eta_2 \partial v_2/\partial z \sim \eta_2 v_i/\ell_w \sim 5 \times 10^{-3}$ Pa, which is much smaller than the stress in the oil phase. Neglecting this last contribution, we get

$$\frac{d\gamma}{dr} + \eta_1 \frac{\partial v_1}{\partial z} = 0 \quad \text{for } z = -d + h_2. \tag{6}$$

This assumption allows to decouple the flows in both phases and to solve analytically the problem. It limits the validity domain of the model to viscous oils, as discussed in the next section.

By successive integrations of Eq. (3), we obtain the velocity field and the radial flux q_1, using the boundary condition Eq. (4):

$$\frac{\partial v_1}{\partial z} = \frac{\rho_1 g}{\eta_1} \frac{dh_1}{dr} (z - h_1), \tag{7}$$

$$v_1 = \frac{\rho_1 g}{2\eta_1} \frac{dh_1}{dr} (z - h_1)^2 + K, \tag{8}$$

$$q_1 = \int_{h_2 - d}^{h_1} v_1 dz = \frac{\rho_1 g}{6\eta_1} \frac{dh_1}{dr} \delta^3 + K\delta, \tag{9}$$

with $\delta = h_1 - h_2 + d$ and K an integration constant.

The order of magnitude of the flux $q_1(r)$ can be estimated from the bump shape evolution. The mass conservation implies

$$q_1(r) = -\frac{1}{2\pi r} \frac{d\Omega(r)}{dt}, \tag{10}$$

with $\Omega(r)$ the oil volume at a distance smaller than r of the z axis. During the quasisteady regime, $d\Omega(r)/dt = 0$ for $r < R$ and it is of the order of $-2\pi h_2 R \, dR/dt$ for $r > R$. The flux q_1 is thus maximal (in absolute value) at $r = R$ and scales as $h_2 dR/dt \approx 10^{-5}$ m^2/s, with $dR/dt \approx -2$ mm/s from Fig. 5(b).

Additionally, the boundary condition at the oil-water interface Eq. (6) provides a relation between the surface tension gradient and the height gradient:

$$\rho_1 g \frac{dh_1}{dr} \delta = \frac{d\gamma}{dr}. \tag{11}$$

This relation provides the profile h_1 as a function of the local surface tension and the local film thickness δ. We find that h_1 is negative and of order of magnitude $h_{1,\text{max}} = \Delta\gamma/[\rho_1 g(d - h_2)] = 0.5$ mm.

We define $A = \frac{\rho_1 g}{6\eta_1} \frac{dh_1}{dr} \delta^3$ the term appearing in Eq. (9). From Eq. (11), we get $A = d\gamma/dr\delta^2/(6\eta_1)$ of the order of 10^{-4} m^2/s, i.e., one order of magnitude larger than q_1. The flux q_1, which would be zero in a steady regime, can thus be neglected in Eq. (9). This justifies to describe this regime as a quasisteady regime. We finally get $K\delta \approx -A$ and

$$K = -\rho_1 g d_r h_1 \delta^2/(6\eta_1). \tag{12}$$

From Eqs. (8), (12), and (11) we can express the oil velocity as a function of the surface tension gradient

$$v_1 = \frac{1}{6\,\delta\,\eta_1} \frac{d\gamma}{dr} [3(z - h_1)^2 - \delta^2], \tag{13}$$

and the interface velocity at the oil-water interface,

$$v_i = \frac{1}{3\,\eta_1} \frac{d\gamma}{dr} \delta. \tag{14}$$

Using $d\gamma/dr \approx \Delta\gamma/R$ we deduce that this velocity is of the order of 1 cm/s, consistently with the experimental observations. To summarize, the oil is pulled outward along the oil-water interface by the Marangoni force. During the quasisteady regime, the oil-air interface is sufficiently deformed so that the hydrostatic pressure induces an inward counter flux that just balances the Marangoni flux. The resulting velocity field v_1 is shown in Fig. 6.

C. Profile of the water-oil interface

The prediction of $h_2(r)$, which is much larger than $h_1(r)$, is surprisingly governed by the hydrostatic law only, despite the relatively large velocities in the water phase. This can be shown by a careful analysis of the order of magnitude of each pressure terms involved in the circulation of the pressure gradients along the closed loop depicted in Fig. 6, written as

$$-\rho_2 g[L + h_2(r)] + \Delta P_{AB}^{\mathrm{dyn}} + \Delta P_B^{\mathrm{cap}} - \rho_1 g\delta + \Delta P_C^{\mathrm{cap}} + \rho_1 gd + \rho_2 gL + \Delta P_{GH}^{\mathrm{dyn}} + \Delta P_{HA}^{\mathrm{dyn}} = 0,$$

$$(\rho_1 - \rho_2)gh_2(r) - \rho_1 gh_1(r) + \Delta P^{\mathrm{dyn}} + \Delta P^{\mathrm{cap}} = 0. \tag{15}$$

This total circulation is zero, as it is the integration of a gradient along a close loop. Along each segment, the pressure difference is decomposed into the hydrostatic part and the dynamical part written ΔP^{dyn}. We only consider this term for the segments in water, as the dynamical contribution of the pressure in the oil phase has been shown to be negligible in the previous section. ΔP^{cap} is the global contribution of the Laplace pressure jumps. The orders of magnitude determined below show that both ΔP^{dyn} and ΔP^{cap} are negligible.

The radial flux (per unit length in the orthoradial direction) in the water phase boundary layer scales as $q_\ell = v_i \ell_w \sim 10^{-5}$ m²/s. Further away from the interface, an inwards counterflow ensures the mass conservation of the water phase. Its relevant vertical characteristic length ℓ_2 can be either the water layer thickness $H = 10$ cm or the bump radius $R \sim 5$ cm. As they are of the same order, we assume $\ell_2 = R$ in the following. As the inward radial flux $q_{\mathrm{in}} = U_2 \ell_2$ must balance q_ℓ we get U_2 of the order of the mm/s as expected. The Reynolds number associated to this counter flow is Re $= \rho_2 R U_2 / \eta_2 \sim 250$, so the dynamical pressure at the origin of the flow scales as $\Delta P^{\mathrm{dyn}} \sim \rho_2 U_2^2 \sim 10^{-2}$ Pa.

Finally, $h_1(r)$ is of the order of 0.5 mm so the order of magnitude of ΔP^{cap} can be estimated as $\Delta P_C^{\mathrm{cap}} \sim -\gamma_{\mathrm{OA}} h_1 / R^2 \sim 2.5\ 10^{-4}$ Pa and $\Delta P_B^{\mathrm{cap}} \sim \gamma_0 h_2 / R^2 \sim 10^{-4}$ Pa.

These values must be compared with the gravitational contribution $\rho_1 gh_1 \approx 5$ Pa, which is much larger. The dynamical and capillary terms are thus negligible and Eq. (15) becomes

$$h_2(r) = -\frac{\rho_1}{\rho_2 - \rho_1} h_1(r). \tag{16}$$

These results express the fact that, in our experimental regime, the water motion is driven by negligible forces. The oil-water interface thus simply follows the oil-air interface deformation, imposed by the Marangoni flows in the oil phase, to maintain the hydrostatic pressure field in the water phase. Consequently, the oil-water interface deformation is an inverted image of the oil-air interface deformation, with a magnification coefficient $\rho_1/(\rho_2 - \rho_1) \sim 10$.

Inserting Eq. (16) in Eq. (11), we obtain

$$\frac{\partial \gamma}{\partial r} = \frac{\rho_1}{2\rho_2} \Delta\rho g \frac{\partial}{\partial r}\left(d - \frac{\rho_2}{\rho_1}h_2\right)^2,$$ (17)

$$\gamma(r) = \gamma_{\text{OW}} - \frac{\rho_1}{2\rho_2} \Delta\rho g \left\{ d^2 - \left[d - \frac{\rho_2}{\rho_1}h_2(r) \right]^2 \right\}.$$ (18)

This expression predicts that the local, out-of-equilibrium surface tension can be measured by the simple observation of the interface deformation of centimetric order. Such relation has also been established for Marangoni flows driven by thermal gradient in Refs. [27,28] in a different experimental geometry. Equivalently, Eq. (18) can be inverted to obtain a prediction for $h_2(r)$ as a function of the local surface tension:

$$h_2(r) = \frac{\rho_1}{\rho_2}\left(d - \left\{ d^2 - [\gamma_{\text{OW}} - \gamma(r)]\frac{2\rho_2}{g\rho_1\Delta\rho} \right\}^{1/2} \right).$$ (19)

For small enough deformations, a Taylor expansion leads to the simpler expression:

$$h_2(r) = \frac{\gamma_{\text{OW}} - \gamma(r)}{gd\Delta\rho}.$$ (20)

At the position $r = 0$, the surface tension is the one of the injected drop, i.e., γ_0, and the height of the bump is maximal:

$$h_{2,\text{max}} = \frac{\rho_1}{\rho_2}\left[d - \left(d^2 - \frac{2\Delta\gamma\rho_2}{g\rho_1\Delta\rho} \right)^{1/2} \right].$$ (21)

At large d, a simplified expression is $h_{2,\text{max}} \approx \Delta\gamma/(gd\Delta\rho)$, consistently with Eq. (20).

The maximal height depends on the surfactant concentration field only through the global surface tension difference $\Delta\gamma$. This explains the presence of the plateau in the graph Fig. 3(a), which lasts as long as the surfactant concentration at $r = 0$ remains larger than the cmc. In contrast, the bump width depends on the whole distribution $\gamma(r)$ and slowly varies with time [see Fig. 3(a)].

Dewetting occurs when $h_{2,\text{max}}$ reaches its critical value $h_{2,\text{max}} = d + h_1(0)$. Using Eq. (16), this leads to $h_{2,\text{max}} = d\,\rho_1/\rho_2$. From Eq. (21), we obtain the critical oil-layer thickness for dewetting

$$d_c^{\text{theo}} = \sqrt{\frac{2\Delta\gamma\rho_2}{g\rho_1\Delta\rho}}.$$ (22)

Finally, the outcomes of this model are the quantitative predictions of a small deformation downward of the upper oil-air interface h_1, and a large deformation upward of the oil-water interface h_2, which is simply the inverted image of h_1, with a magnification factor $\rho_1/(\rho_2 - \rho_1)$. This factor can become very large if the density of the two phases are close enough and makes the deformation of the water-oil interface much easier to observe than the one of the oil-air interface. If the oil phase is viscous enough, the local surface tension at the oil-water interface is related to this deformation by a simple analytical expression.

V. COMPARISON WITH EXPERIMENTS

First, the modelization provides predictions which are qualitatively in agreement with our observations and explains these nonintuitive behaviors. The fact that the water bump is rising upward turns out to be a direct consequence of the small downward deformation of the oil-air interface. As well, the magnification factor $\rho_1/(\rho_2 - \rho_1)$ is crucial as it allows us to easily visualize h_2, while h_1 is impossible to see with eyes.
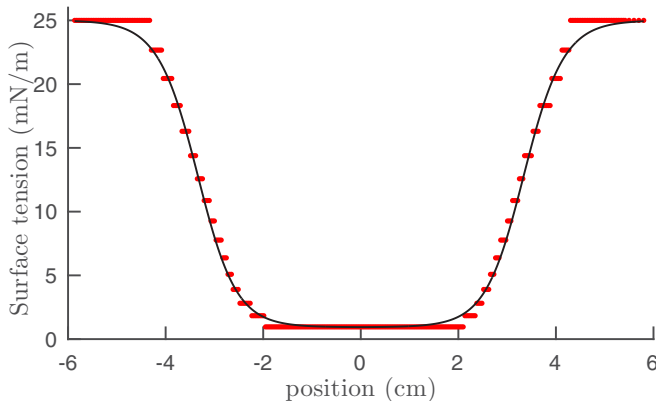
FIG. 7. Surface tension profile deduced from the interface deformation shown in Fig. 4, using Eq. (18). The error bar is given by the vertical distance between the red dots. The black line is obtained from the smooth fit of the interface profile Eq. (1), whereas the red dots are obtained from the raw data.

Quantitatively, we can first compare the critical oil-layer thickness leading to the dewetting transition. For the sunflower oil, all the physical quantities in the right-hand side of Eq. (22) have been measured, and their values are reported in Table I. Using these values we get the prediction $d_c^{\text{theo}} = 8.2$ mm, in good agreement with our experimental observation $d_c = 8 \pm 1$ mm.

For further comparisons, complementary experiments have been performed with different oils. With V10 of viscosity $\eta^{V10} = 10$ mPa s, we obtained $d_c/d_c^{\text{theo}} = 0.95$, again in good agreement. However, with hexadecane of viscosity $\eta^{\text{hex}} = 3$ mPa s, a significant difference between theoretical and experimental results occurs. Indeed we get $d_c/d_c^{\text{theo}} = 0.6$. It then seems that the critical oil viscosity below which the flow decoupling assumed in Eq. (6) is no longer valid is thus of the order of few mPa s.

We also increased the drop volume and checked that the critical thickness is independent of this parameter. However, if the drop becomes too small, or not concentrated enough, the dewetting transition occurs for a smaller oil thickness value. This is consistent with a lower value of $\Delta\gamma$, if the drop does not ensure a local concentration above the CMC.

For oil thicknesses above the critical value d_c, we can also test Eq. (21), which provides a prediction for the maximal deformation height as a function of d. This prediction is plotted in Fig. 5 and is in a quantitative agreement with the experimental data. Note that the fitting is done with no adjustable parameters.

Following the agreement between the data and the model shown in Fig. 5, our more general prediction [Eq. (19)] can therefore be used to determine the dynamical surface tension profile over the whole oil-water interface, using its reciprocal form Eq. (18). This prediction assumes that the surface tension at large r is at its equilibrium value γ_{OW} and deduces the surface tension at any other radial position from the oil-water interface deformation. We present in Fig. 7 the surface tension distribution obtained from the interface profile shown in Fig. 4.

As already proved by Fig. 5, the predicted value for the oil-water surface tension at $r = 0$ agrees with the lowest possible value of the surface tension γ_0 (the one found above the cmc and independently measured). The other surface tension values, at intermediate r, cannot be compared to other experimental data: it is impossible to accurately resolve in space the dynamical surface tension with conventional techniques, as we have done here with this new approach.

VI. CONCLUSION

We present a surfactant-spreading experiment at the oil-water interface. Under the Marangoni stress, we measure and explain that a water bump rises oppositely to the gravity, with a vertical

amplitude that depends on the oil-layer thickness. In the case of no dewetting, we provide an analytical expression relating the vertical oil-water interface deformation to the in-plane local surface tension. The dynamical surface tension generated by a flow in a diphasic system with surfactants is almost impossible to measure with conventional techniques. Our setup allows us to have an indirect, but simple, optical measurement of the out-of-equilibrium surface tension, for steady or quasisteady regimes. More importantly, this technique takes advantage of a magnification effect scaling as $\rho/\Delta\rho$ ($\Delta\rho$ being the density difference between the two phases), which amplifies the oil-water interface deformation. This density difference can be adjusted to very small values in order to measure tiny surface tension variations. The model can be extended to the case of surface tension gradients created at the oil-air interface and leads to the same conclusions. Preliminary tests with an oil soluble surfactant deposited at the oil-air interface have indeed evidenced a rising bump at the water-oil interface. We thus believe that this two fluid layers setup may be used as an efficient tensiometry technique for a large class of steady Marangoni flows. Finally, for small thicknesses, the water bump grows so much that it pierces the oil layer, inducing a Marangoni-driven liquid-liquid dewetting. The hole open in the oil layer can last up to hours. The origins of this stability, linked to the trapping of insoluble species at the water-air interface, and other properties and perspectives of this experimental configuration will be discussed in a forthcoming paper.

[1] C. Marangoni, Ueber die ausbreitung der tropfen einer flüssigkeit auf der oberfläche einer anderen, Ann. Phys. **219**, 337 (1871).

[2] L. E. Scriven and C. V. Sternling, The Marangoni effects, Nature **187**, 186 (1960).

[3] Y. K. Bratukhin and L. N. Maurin, Thermocapillary convection in a fluid filling a half-space, J. Appl. Math. Mech. **31**, 605 (1967).

[4] J. P. Longtin, K. Hijikata, and K. Ogawa, Laser-induced surface-tension-driven flows in liquids, Int. J. Heat Mass Transfer **42**, 85 (1999).

[5] M. F. Schatz and G. P. Neitzel, Experiments on thermocapillary instabilities, Annu. Rev. Fluid. Mech. **33**, 93 (2001).

[6] A. I. Mizev, Experimental investigation of thermocapillary convection induced by a local temperature inhomogeneity near the liquid surface. 2. Radiation-Induced Source of Heat, J. App. Mech. Tech. Phys. **45**, 699 (2004).

[7] H. Chraïbi and J.-P. Delville, Thermocapillary flows and interface deformations produced by localized laser heating in confined environment, Phys. Fluids **24**, 032102 (2012).

[8] O. E. Jensen and J. B. Grotberg, Insoluble surfactant spreading on a thin viscous film: Shock evolution and film rupture, J. Fluid Mech. **240**, 259 (1992).

[9] M. R. E. Warner, R. V. Craster, and O. K. Matar, Fingering phenomena associated with surfactant spreading on thin liquid films, J. Fluid Mech. **510**, 169 (2004).

[10] A. D. Dussaud, O. K. Matar, and S. M. Troian, Spreading characteristics of an insoluble surfactant film on a thin liquid layer: Comparison between theory and experiment, J. Fluid Mech. **544**, 23 (2005).

[11] O. K. Matar and R. V. Craster, Dynamics of surfactant-assisted spreading, Soft Matter **5**, 3801 (2009).

[12] D. Suciu, O. Smigelschi, and E. Ruckenstein, The spreading of liquids on liquids, J. Colloid Interface Sci. **33**, 520 (1970).

[13] D. Halpern and J. B. Grotberg, Dynamics and transport of a localized soluble surfactant on a thin film, J. Fluid Mech. **237**, 1 (1992).

[14] O. E. Jensen and J. B. Grotberg, The spreading of heat or soluble surfactant along a thin liquid film, Phys. Fluids A—Fluid **5**, 58 (1993).

[15] K. Lee and V. Starov, Spreading of surfactant solutions over thin aqueous layers at low concentrations: Influence of solubility, J. Colloid Interface Sci. **329**, 361 (2009).

[16] M. Roché, Z. Li, I. M. Griffiths, S. LeRoux, I. Cantat, A. Saint-Jalmes, and H. A. Stone, Marangoni Flow of Soluble Amphiphiles, Phys. Rev. Lett. **112**, 208302 (2014).

[17] S. Le Roux, M. Roché, I. Cantat, and A. Saint-Jalmes, Soluble surfactant spreading: How the amphiphilicity sets the Marangoni hydrodynamics, Phys. Rev. E **93**, 013107 (2016).

[18] V. Pimienta and C. Antoine, Self-propulsion on liquid surfaces, Curr. Opin. Colloid Interface Sci. **19**, 290 (2014).

[19] S. Nakata, M. Nagayama, H. Kitahata, N. J. Suematsu, and T. Hasegawa, Physicochemical design and analysis of self-propelled objects that are characteristically sensitive to environments, Phys. Chem. Chem. Phys. **17**, 10326 (2015).

[20] R. Stocker and J. W. M. Bush, Spontaneous oscillations of a sessile lens, J. Fluid Mech. **583**, 465 (2007).

[21] J. F. Hernández-Sánchez, A. Eddi, and J. Snoeijer, Marangoni spreading due to a localized alcohol supply on a thin water film, Phys. Fluids **27**, 032003 (2015).

[22] S. M. Troian, X. L. Wu, and S. A. Safran, Fingering Instability in Thin Wetting Films, Phys. Rev. Lett. **62**, 1496 (1989).

[23] M. R. E. Warner, R. V. Craster, and O. K. Matar, Fingering phenomena created by a soluble surfactant deposition on a thin liquid film, Phys. Fluids **16**, 2933 (2004).

[24] A. Hamraoui, M. Cachile, C. Poulard, and A. Cazabat, Fingering phenomena during spreading of surfactant solutions, Colloids Surf. A **250**, 215 (2004).

[25] L. Keiser, H. Bense, P. Colinet, J. Bico, and E. Reyssat, Marangoni Bursting: Evaporation-Induced Emulsification of Binary Mixtures on a Liquid Layer, Phys. Rev. Lett. **118**, 074504 (2017).

[26] See Supplemental Material at http://link.aps.org/supplemental/10.1103/PhysRevFluids.3.024003 for a movie of the Marangoni flows in the vertical plan.

[27] M. Robert de Saint Vincent, H. Chraïbi, and J. P. Delville, Optical Flow Focusing: Light-Induced Destabilization of Stable Liquid Threads, Phys. Rev. Appl. **4**, 044005 (2015).

[28] D. Rivière, Ecoulements thermogravitaires et thermocapillaires induits par chauffage laser dans des couches liquides, Ph.D. thesis, Université de Bordeaux, 2016.